TURBULENCE INVESTIGATION OF THE NASA COMMON RESEARCH MODEL WING TIP VORTEX

by

Đorđe S. ČANTRAK[1*], James T. HEINECK[2], Laura K. KUSHNER[3], and Novica Z. Janković[1]

[1] Department of Aerospace Engineering, Faculty of Mechanical Engineering, University of Belgrade, Belgrade, Serbia
[2] NASA Ames Research Center, Experimental Aero-Physics Branch, Moffett Field, CA 94035 USA
[3] AerospaceComputing, Inc, Mountain View, CA 94043 USA

Original scientific paper
DOI: ???

The paper presents high-speed stereo particle image velocimetry investigation of the NASA Common Research Model wing tip vortex. A three-percent scaled semi-span model, without nacelle and pylon, was tested in the 32- by 48- inch Indraft Tunnel, at the Fluid Mechanics Laboratory at the NASA Ames Research Center. Turbulence investigation of the wing tip vortex is presented. Measurements of the wing-tip vortex were performed in a vertical cross-stream plane three tip-chords downstream of the wing tip trailing edge with a 2 kHz sampling rate. Experimental data are analyzed in the invariant anisotropy maps for three various angles of attack (0°, 2° and 4°) and the same speed generated in the tunnel (V_∞ = 50 m/s). This corresponds to a chord Reynolds number $2.68 \cdot 10^5$, where the chord length of 3" is considered the characteristic length. The region of interest was x = 220 mm and y = 90 mm. The 20 000 particle image velocimetry samples were acquired at each condition. Velocity fields and turbulence statistics are given for all cases, as well as turbulence structure in the light of the invariant theory. Prediction of the wing tip vortices is still a challenge for the computational fluid dynamics codes due to significant pressure and velocity gradients.

Key words: *turbulence, invariant maps, vortex, high-speed stereo PIV, CRM*

Introduction

Experimental and numerical investigations of the NASA Common Research Model (CRM) still capture the attention of many researchers worldwide. It was developed as an open-source contemporary transonic supercritical wing for various studies in aerodynamics, as reported in [1]. Numerous experimental and numerical investigations have been performed since 2008 [1-12]. Literature overview of interest is provided in [10].

Study of the wake of NASA CRM Model in European Transonic Wind tunnel (ETW), under high Re-number stall conditions for sub- and transonic speeds, with high-speed particle image velocimetry (HS PIV) is presented in [11]. Comparison of the NASA CRM test data in ETW to NASA test data obtained in the NASA Langley National Transonic Facility is

* Corresponding author; e-mail: djcantrak@mas.bg.ac.rs

given in [12]. Also, in [12] the force and moment, surface pressure and wing bending and twist data are presented.

Experimental test rig

Experiments were conducted in the 32- by 48- inch Indraft Tunnel, located at the FML (Fig. 1.). The tunnel test section is 10 ft. (3.048 m) long, 4 ft. (1219.2 mm) wide and 32 in. (app. 813 mm) high, and is transparent on two sides. A freestream turbulence level is 0.15%. Temperature, relative humidity and atmospheric pressure are measured while the tunnel is operational. A description of the FML 32"×48" wind tunnel is provided in [10, 13].

The NASA CRM model geometry and experimental results are available online in [14]. For these experiments the trip dots 0.0114" or 0.2896 mm in diameter at 2.54 mm spacing were applied to the wing at 10% of the chord away from the leading edge. This was performed after flow visualization experiments to induce transition and reduce the possibility of separation and sensitivity to the incoming flow. Figure 1.a shows a diagram of the semi-span CRM model in the test section. Figure 1.b displays the position of the cameras (outside the measurement area), while CRM and calibration target are inside the test section.

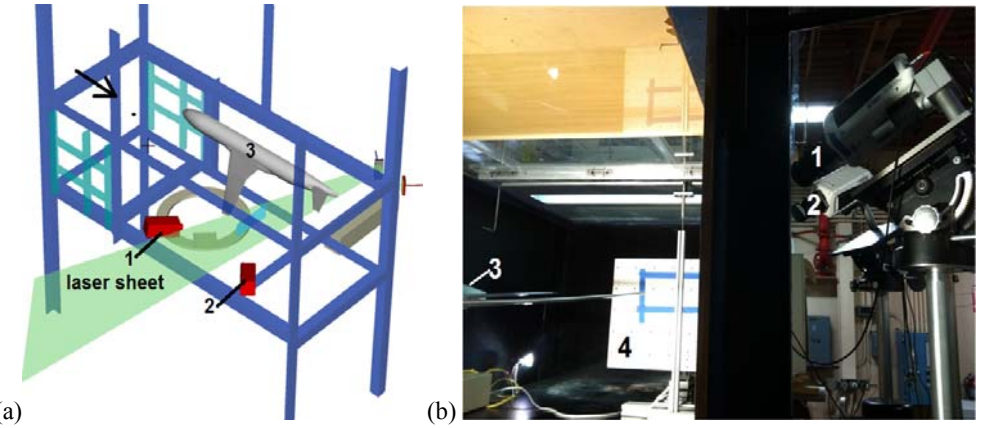

(a) (b)

Figure 1. a) A 3% scaled semi-span Common Research Model (CRM) in wind tunnel: 1-left and 2-right CMOS cameras and 3-CRM, b) 1 and 2- CMOS cameras, 3-CRM and 4-target.

The CRM was mounted on the wind tunnel wall at the angles of attack: 0°, 2° and 4°. The CRM dimensions and position in wind tunnel are specified in [10], as well as in fig. 2.a. The HSS PIV system calibration setup is shown in figs. 1.b and 2.a. Some details, concerning the region of interest (ROI), are presented in fig. 2.b. Measurements were taken in a vertical cross-stream plane three tip-chords downstream of the wing tip trailing edge - 9.6" or 243.84 mm, which corresponds to the origin of the coordinate system, where the z-axis is directed downstream with the fluid flow.

The height of the wing tip trailing edge from the test section bottom was checked for each angle of attack. It is assumed that only this dimension changes. The height varied from 427.1 mm for $\alpha = 0°$ (fig. 2.b), 411.2 mm for $\alpha = 2°$ and 393.7 mm for $\alpha = 4°$.

An optimal HSS PIV arrangement was designed using test-planning visualization software (fig. 1.a and fig. 2.b) [15]. The HSS PIV experimental setup is presented in fig. 1. A

double-pulsed Nd:YLF laser (Quantronix Darwin-Duo) with 527 nm and average power greater than 100 W at 3 kHz illuminated the flow.

(a) 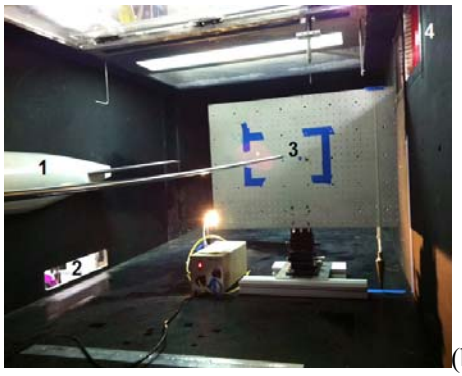

(b) 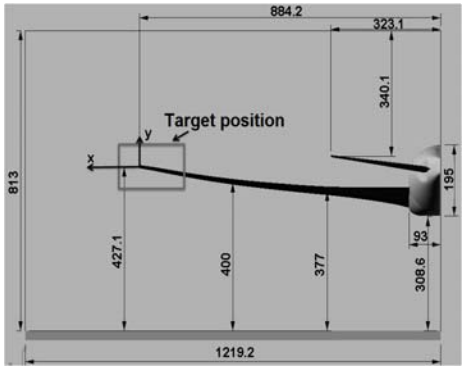

Figure 2. CRM at test section: a) HSS PIV calibration setup for angle of attack 2°: 1-CRM, 2-laser sheet inlet window, 3-calibration target and 4-window for CMOS cameras, b) view from behind - position of the wing tip trailing edge point for angle of attack 0° and ROI (All dimensions are in millimeters).

The operating frequency during experiments was 2 kHz with pulse spacing of the order of 10 μs. The laser sheet was shaped using spherical and cylindrical lenses and was directed to the ROI by a set of mirrors through a window (fig. 2.a). The laser sheet thickness in the ROI was approximately 1 mm.

Two high-speed 12-bit CMOS cameras, Phantom v641s, were oriented to a nearly forward scatter arrangement from the opposite sides of the laser sheet (fig. 1). The cameras operated at 4 kHz with window size 1600 × 700 pixels. Two-axis Scheimpflug focusing was required to achieve perfect sharpness of the laser light sheet plane while using a large aperture in the lens (fig. 1.b). The obtained dimensions of ROI were x = 220 mm and y = 90 mm. Ten runs were obtained for each angle of attack and 2088 image pairs per camera for each run were recorded. Each run spans 1.044 s. The flow was seeded with 0.7 μm to 1 μm oil droplets that were injected just upstream of the tunnel inlet [10].

Experimental results and analysis

The wind tunnel speed was approximately the same for all measurements near V_∞ = 50 m/s, or 49.9 m/s for α = 0° and α = 2°, while 50.15 m/s for α = 4°. A chord Reynolds number, calculated on the basis of the wing tip chord length (3.2", i.e. 81.28 mm) is $Re_C \approx 2.68 \cdot 10^5$.

Calibration, data acquisition and processing were performed using DaVis software by La Vision. Time-averaged velocity components (V_i, where i = x, y and z) and averaged vorticity (Ω_i, where i = x, y and z) were determined on the basis of the measured instantaneous velocity fields. In addition, velocity fluctuations (v_i, where i=x, y and z) and stresses were calculated on the basis of the measured velocity fields in DaVis software. Invariant maps and turbulent kinetic energy were determined by in-house code.

All three velocity components were reconstructed in the ROI in the following way. The stereo cross-correlation was applied using multi-pass iterations starting with the size of the interrogation window 96 × 96 pixels in one pass and 50% overlap down to three passes

with a final window size of 32 × 32 pixels and 75% overlap. Median filtering was applied and smoothing at a windows size of 3 × 3. All three velocities were accepted if stereo reconstruction error was less than 5 pixels. Missing vectors were interpolated. Exactly, 17 661 points with the step of 1.111 mm in the x-axis direction and 1.115 mm in the y-direction were generated in each data run [10].

Velocity fields

The ensemble averaged total velocity fields (V_e) for all angles of attack are presented in [10]. Figure 3. presents the total velocity field for one run out of ten for each angle of attack.

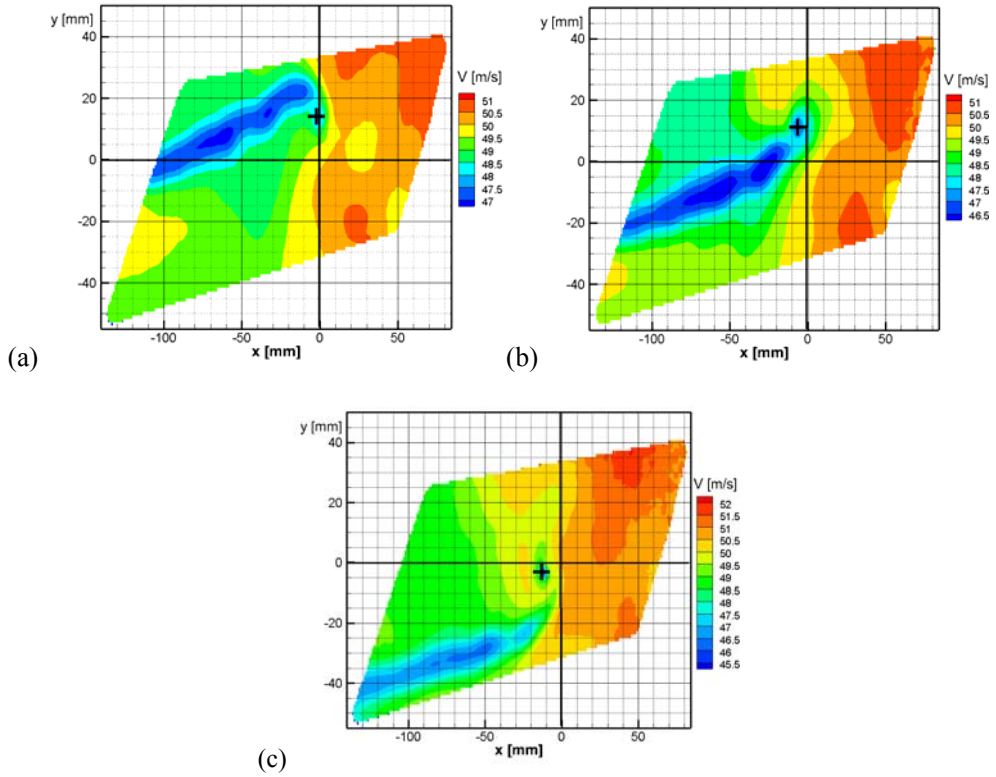

Figure 3. Total velocity fields for angle of attack (α): a) 0°, b) 2° and c) 4°. Note: White cross denotes the vortex core position.

One data set includes 2088 image pairs for each camera, which generates three-component velocity fields (V_x, V_y and V_z). The ensemble averaged velocities ($V_{x,e}$, $V_{y,e}$ and $V_{z,e}$) are formed on the basis of ten completely independent, i.e. stochastic data sets (20 880 image pairs), as well as the ensemble averaged total velocity fields (V_e).

On the basis of averaged total velocity field and ensemble averaged total velocity field, it was shown that flow for all angles of attack could be treated as statistically stationary [10].

The vortex core is identified as the total velocity minimum in the vortex core region. Its position is x = -1.25123 mm and y = 13.8945 mm for α = 0° (fig. 3.a). It is obvious that the wing tip vortex circulates counterclockwise as viewed from downstream. It is the direction opposite to that for a wing creating a positive lift [10]. The total velocity reached at this point is V = 47.86 m/s, and although this is not the lowest velocity in the entire measured area, it is the lowest in the region of the vortex core. For α = 2° the vortex core has the coordinates x = -6.80899 mm, y = 11.6714 mm (fig. 3b), while for α = 4° they are x = -12.3667 mm, y = -2.77881 mm (fig. 3.c). The achieved total velocity in the vortex core is V = 47.0561 m/s for α = 2°, while it is V = 45.8836 m/s for α = 4°. The second value is the total velocity minimum in the entire measurement area. These points are not aligned with the wing tip profile end point. The direction of circulation at higher angles of attack is reversed and consistent with a lifting wing.

Vortex sheets are obvious in fig. 3. The total velocity minima are reached for α = 0° and 2° inside the vortex sheet, while for α = 4° the velocity minimum is exactly in the vortex core center.

It was shown in [10] that both cross-stream velocities (V_x and V_y) have small values compared to the dominant axial velocity (V_z) for all angles of attack and data runs, so they are not presented here.

The average of ten vorticity fields ($\Omega_{z,e}$), obtained from ten averaged vorticity fields, for all three angles of attack are calculated and presented in [10]. It was shown that the maximum streamwise vorticities are obtained in the same points, where total velocity minima occur and the highest streamwise vorticity is reached for α = 4°. Vortex sheets are identified for all three angles of attack with higher vorticities [10].

Investigations by using invariant maps

The state of turbulence is analyzed by the amount of anisotropy in the flow [17]. Components of the nondimensional anisotropy tensor , as a measure of turbulence, are introduced as:

$$a_{ij} = \frac{1}{2k}\overline{v_i v_j} - \frac{1}{3}\delta_{ij}, \tag{1}$$

where $k = \frac{1}{2}\left(\overline{v_x^2} + \overline{v_y^2} + \overline{v_z^2}\right)$ is TKE and δ_{ij} is Kronecker delta [18,19].

In the case of isotropic turbulence all components of tensor vanish (a_{ij}=0). Other states of turbulence anisotropy are analyzed on the basis of aij values. Paper [20] discusses possible states of turbulence, i.e. trajectories of joint variation of invariants for incompressible turbulent channel flow. It is shown in [17] that high degrees of turbulent anisotropy occur in the region dominated by the oscillating vortex core. The invariant theory for the HSS PIV study of the turbulent swirl flow behind the axial fan in a pipe is applied in [16,21]. Scalar functions of the components of the anisotropy tensor present the first, second and third invariant of the second order tensors in the following way:

$$I_a = 0,\ II_a = -\frac{1}{2}a_{ij}a_{ji},\ III_a = \frac{1}{3}a_{ij}a_{ik}a_{jk}. \tag{2}$$

Experimentally determined scalar invariants II_a and III_a are presented in III_a-($-II_a$) plane, i.e. in anisotropy invariant maps (fig. 4.) for all three angles of attack. It seems that the turbulence states tend to isotropy for $\alpha = 2°$ and $\alpha = 4°$, which is not the case for $\alpha = 0°$.

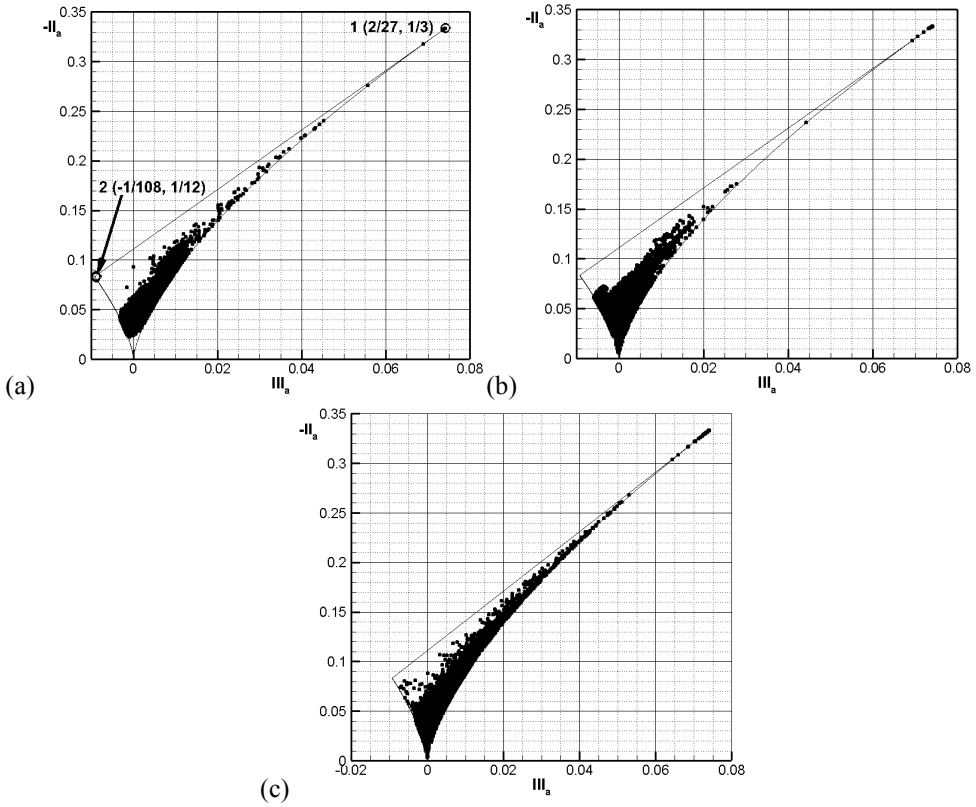

Figure 4. Anisotropy invariant maps for angles of attack (α): a) 0°, b) 2° and c) 4°.

All possible states of turbulence anisotropy belong to the curvilinear triangle area (012), called the Lumley triangle or anisotropy invariant map. Frontiers of the invariant map, which describe the border states of turbulence, are defined in [18] as follows:

$$201:\ -II_a = \frac{3}{4}(4|III_a|)^{2/3} + \frac{1}{9} \text{ and } \overline{21}:\ -II_a = 3III_a + \frac{1}{9} \tag{3}$$

here 201 denotes axisymmetric turbulence states (two components are equal in magnitude), 20 stands for axisymmetric contraction (one component of the velocity fluctuations is smaller than the other two), 01 for axisymmetric expansion (one component dominates over the other two) and 21 for two-component turbulence (one component of the velocity fluctuations is negligible compared to the other two). Lumley triangle vertices (fig. 4.a) correspond to turbulence boundary conditions: 0 (IIa = IIIa = 0) - three-component isotropic turbulence, point 1 describes boundary layer of one-component isotropic turbulence and 2 corresponds to two-component isotropic turbulence. These two invariants are calculated for one data set for each

angle of attack, for all 10 075 measured points. All these points belong to the domain of the invariant map and describe various turbulence states that are physically possible. Most of the points, for all angles, are distributed in the right part of the invariant map (IIIa > 0) and along the line 01 which characterizes the turbulence state of the axisymmetric expansion. This region is characterized by one fluctuating component dominating the other two. It is evident (fig. 4) that in the case of $\alpha = 0°$ and $\alpha = 2°$ points don't reach the three-component isotropic turbulence state, but this is achieved for $\alpha = 4°$. The left part of the map (IIIa < 0) denotes axisymmetric turbulence, where one component is smaller than the other two. Lower number of points lay in this region for all angles.

Figure 5. shows invariant maps along one vertical direction through the vortex core centers for each angle of attack. All points belong to the Lumley triangle, but flow behavior in these points is different. All 59 points have the same y-coordinate. There is one additional point for $\alpha = 2°$ and two points for $\alpha = 4°$. Turbulence states are analyzed by the amount of anisotropy in the flow along the vertical directions in the vortex core x-positions. It is obvious that isotropic turbulence doesn't occur in these directions (fig. 5.). High degrees of turbulent anisotropy occur in the entire region dominated by the wing tip vortex.

If the vortex core is observed as one point in the fluid flow region, invariants are calculated for all three angles. Values $III_a = -0.00108$ and $-II_a = 0.03917$ (fig. 5.a) are obtained for $\alpha = 0°$ in the vortex core, whereas $III_a = 0.00293$ and $-II_a = 0.06943$ (fig. 5.b) for $\alpha = 20$, and for $\alpha = 4°$ the values are $III_a = 0.01368$ and $-II_a = 0.11895$ (fig. 5.c).
.01368 and $-II_a = 0.11895$ (fig. 5.c).

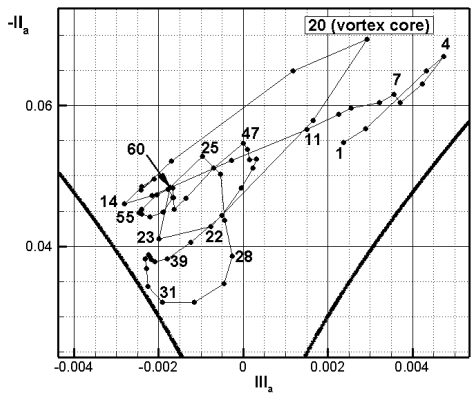

(a)

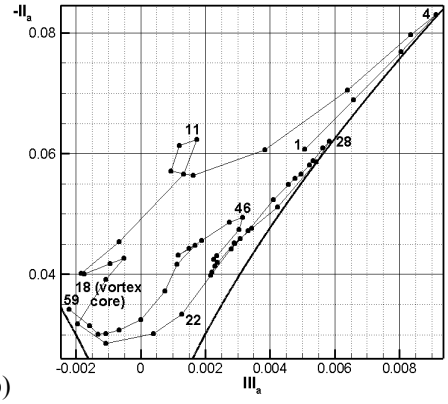

(b)

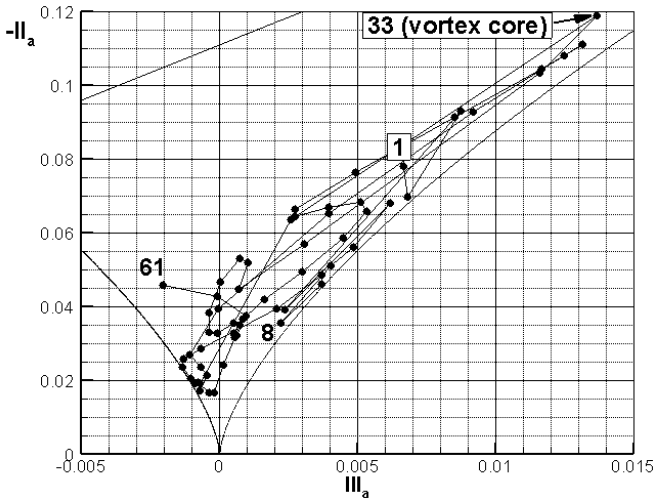

(c)

Figure 5. Anisotropy invariant maps for angles of attack (α) and specified directions: a) 0° and x = -1.25123 mm, b) 2° and x = -6.80899 mm and c) 4° and x = -12.3667 mm.

This resolves a variety of anisotropy behavior of the vortex cores for all three angles. Only in the case of $\alpha = 0°$ the vortex core is closer to the 20 frontier, i.e. axisymmetric contraction, while for other two angles it is closer to axisymmetric expansion.

All three cases reveal that generated vortex cores are highly anisotropic. Most of the points for $\alpha = 0°$ and $\alpha = 4°$ occur in the region of the axisymmetric expansion (01), characterized by one fluctuating component that dominates over the other two. It is opposite for $\alpha = 2°$, where the majority of points are positioned closer to the line 20 that represents axisymmetric contraction.

Positions of total velocity minimum

It was shown in [10] that the vortex core was where the cross-stream velocities changed sign and where the gradients were largest. This provides the same result as the total velocity minimum criterion for defining the vortex core used, as shown in [16].

The criterion of the velocity minimum is applied in studying the wing tip vortex core, as well as the vortex sheet. These points are presented in fig. 6. They resolve the vortex sheets.

It is obvious that the points are predominantly located on the vortex sheet (fig. 6.). Not all the points are unique. In the case for $\alpha = 0°$ only 580 points are visible, while for $\alpha = 2°$ 689 points. Most of them are not unique and this is shown in histograms in fig. 7. The number of repetitions varies for different angles and positions.

In the case for $\alpha=0°$ the number of unique points is 211, that is, 36.4% of all visible points, for $\alpha = 2°$ their number is 288, that is, 41.8% and for $\alpha = 4°$ it is 518, what makes up 58.9%. It is obvious that the highest number of repetitions is achieved along the vortex sheet. The highest repetition number of 185 is achieved for $\alpha = 4°$ in app. vortex core center. The highest repetition number for other two angles is only 20 for $\alpha = 0°$ and 33 for $\alpha = 2°$. So, it means that the number of unique points, as well as the repetition number increases as the angle of attack increases and reaches maxima for $\alpha = 4°$.

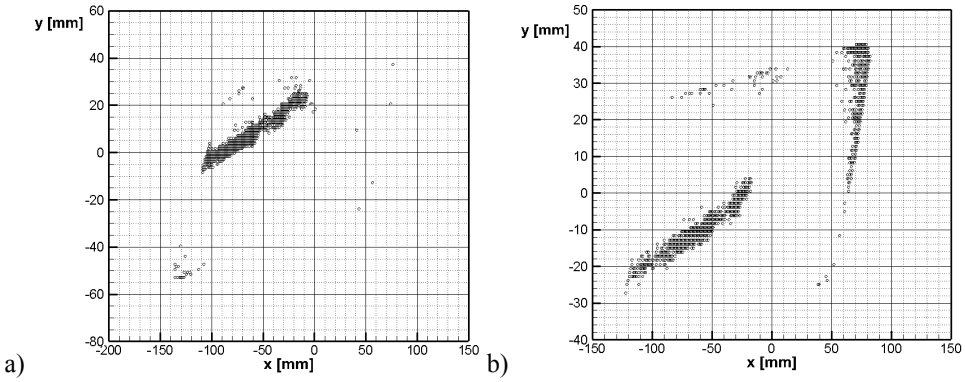

Figure 6. Positions of the velocity minimum for the angles of attack: a) 0° (data set No. 3) and b) 2° (data set No. 3).

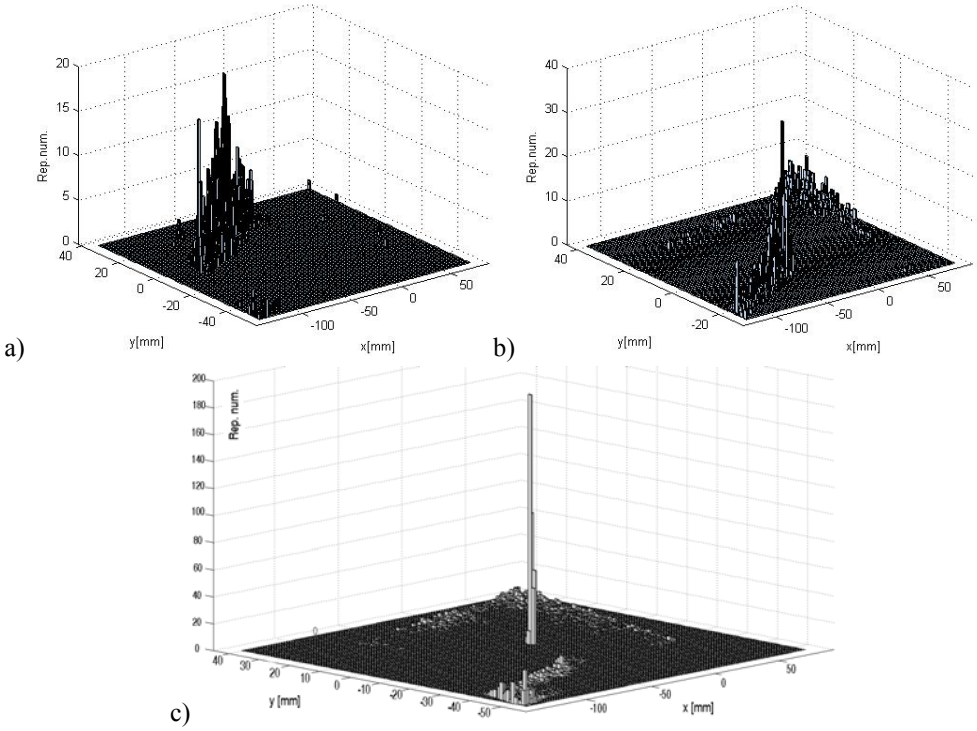

Figure 7. Distributions of the velocity minima repetitions in the measurement plane for the angles of attack: a) 0° (data set No. 3), b) 2° (data set No. 3) and c) 4° (data set No. 4).

Conclusions

This paper studies the wing tip vortex on a 3% scaled semi-span CRM applying the HSS PIV measurement method. Experimental results were obtained in the measurement plane

three cords downstream from the end point of the wing tip profile for all three angles of attack ($\alpha = 0°$, 2° and 4°). Highly turbulent flows are generated. It is shown that the wing tip vortex circulates counterclockwise as viewed from downstream for $\alpha = 0°$. The generated wing tip vortices for $\alpha = 2°$ and $\alpha = 4°$ create positive lift.

Paper [10] indicates that the velocity intensities do not change significantly as a function of the angle of attack flow and the flow could be treated for all three angles of attack as a statistically stationary flow. This is also proved here. It is shown that the positions of the vortex core centers for the studied cases correspond to the ones for the ensemble averaged total velocity fields.

All possible states of turbulence anisotropy of the studied flow for all three angles of attack are investigated in the anisotropy invariant map. Almost all points are grouped in the right part of the Lumley triangle, close to the line 01 that describes the turbulence state of axisymmetric expansion. A high number of points for $\alpha = 2°$ and $\alpha = 4°$ are in the vicinity of the three-component isotropic turbulence (state 0), whereas for $\alpha = 0°$ none of the points approach this state.

The total velocity minima criterion defined vortex sheets for $\alpha = 0°$ and $\alpha = 2°$, but the vortex core for $\alpha = 4°$. The vortex core center is determined as the point of the highest repetition number for $\alpha = 4°$.

Additional HSS PIV measurements in the planes one and two tip-chords downstream of the wing tip are necessary for documenting the streamwise evolution of the wing tip vortex.

Acknowledgements

Author Đorđe Čantrak conducted his research at the NASA Ames FML and Center for Turbulence Research at Stanford University as a Fulbright Visiting Scholar April-June 2013. He expresses his gratitude to Prof. Dr. Peter Bradshaw, Prof. Dr. Parviz Moin, Director of the CTR and Dr. Srboljub Jović for their great support during research. Authors owe special gratitude for support in experimental work to all other FML members, especially Dr. Rabindra Mehta, Experimental Aero-Physics Branch Chief, Edward Schairer, Nettie Halcomb Roozeboom, Kurtis Long and Barry Porter. This CRM wind tunnel test was supported by the NASA Revolutionary Computational Aerosciences (RCA) project. Authors Đorđe Čantrak and Novica Janković also express their gratitude to the Ministry of Education, Science and Technological Development of the Republic of Serbia, Project No. TR 35046.

Nomenclature

V – total velocity , [ms^{-1}]
V_∞ – wind tunnel speed, [ms^{-1}]
V_x – x-component of averaged velocity, [ms^{-1}]
V_y – y-component of averaged velocity [ms^{-1}]
V_z – z-component of averaged velocity, [ms^{-1}]
V_e – ensemble averaged total velocity, [ms^{-1}]
$V_{x,e}$ – x-component of ensemble averaged total velocity, [ms^{-1}]
$V_{y,e}$ – y-component of ensemble averaged total velocity, [ms^{-1}]
$V_{z,e}$ – z-component of ensemble averaged total velocity, [ms^{-1}]
$a_{i,j}$ – components of the nondimensional anisotropy tensor, [–]
Re – Reynolds number (= $\rho vc/\mu$), [–]
k – turbulent kinetic energy, [J]
x – spatial coordinate, [m]
y – spatial coordinate, [m]
z – spatial coordinate, [m]

Greek symbols

α – angle of attack, [º]
δ_{ij} – Kronecker delta function, [–]
ρ – density, [kgm^{-3}]

References

[1] Vassberg, J.C., *et al*., Development of a common research model for applied CFD validation studies, *Proceedings,* 26th AIAA Applied Aerodynamics Conference, Honolulu, Hawaii, AIAA Paper no. 2008-6919.
[2] Acheson, M.J., Balakrishna, S., Effects of active sting damping on common research model data quality, *Proceedings,* 49th AIAA Aerospace Sciences Meeting including the New Horizons Forum and Aerospace Exposition, Orlando, Florida, AIAA Paper no. 2011-878.
[3] Balakrishna, S., Acheson, M.J., Analysis of NASA common research model dynamic data, *Proceedings,* 49th AIAA Aerospace Sciences Meeting including the New Horizons Forum and Aerospace Exposition, Orlando, Florida, AIAA Paper no. 2011-1127.
[4] Bell J.H., Pressure-sensitive paint measurements on the NASA common research model in the NASA 11-ft transonic wind tunnel, *Proceedings*, 49th AIAA Aerospace Sciences Meeting including the New Horizons Forum and Aerospace Exposition, Orlando, Florida, AIAA Paper no. 2011-1128.
[5] Rodi, W., DES and LES of Some Engineering Flows, *Fluid Dynamics Research*, *38* (2006), 2-3, pp. 145-173
[6] Zilliac, G.G., *et al.,* A Comparison of the measured and computed skin friction distribution on the common research model, *Proceedings* 49th AIAA Aerospace Sciences Meeting including the New Horizons Forum and Aerospace Exposition, Orlando, Florida, AIAA Paper no. 2011-1129.
[7] Rivers, M.B., Dittberner A., Experimental investigations of the NASA Common Research Model in the NASA Langley National Transonic Facility and NASA Ames 11-Ft Transonic Wind Tunnel (Invited), *Proceedings,* 49th AIAA Aerospace Sciences Meeting including New Horizons Forum and Aerospace Exposition, Orlando, Florida, AIAA Paper no. 2011-1126.
[8] Rivers, M.B., Hunter, C.A., Support system effects on the NASA common research model, *Proceedings,* 50th AIAA Aerospace Sciences Meeting including the New Horizons Forum and Aerospace Exposition, Nashville, Tennessee, AIAA Paper no. 2012-0707.
[9] Rivers, M.B., *et al*., Further investigation of the support system effects and wing twist on the NASA common research model, *Proceedings*, 30th AIAA Applied Aerodynamics Conference, New Orleans, Louisiana, AIAA Paper no. 2012-3209.
[10] Illi, S.A., *et al.*, Transonic tail buffet simulations for the common research model, Fluid Dynamics and Co-located Conferences, , *Proceedings*, 31st AIAA Applied Aerodynamics Conference, San Diego, CA AIAA Paper no. 2013-2510.
[11] Čantrak, Đ.S., *et al.*, Time-resolved stereo PIV investigation of the NASA Common Research Model in the NASA Ames Fluid Mechanics Laboratory 32- by 48-in indraft wind tunnel, *Annual Research Briefs*, Center for Turbulence Research, Stanford University/NASA Ames, (2014), pp. 179-191.
[12] Konrath, R., *et al*., High-Speed PIV applied to wake of NASA CRM model in ETW under high Re-number stall conditions for sub- and transonic speeds, *Proceedings,*53rd AIAA Aerospace Sciences Meeting, AIAA SciTech, Kissimmee, Florida, AIAA 2015-1095.
[13] Rivers, M.B., *et al.*, Comparison of the NASA Common Research Model European Transonic Wind Tunnel Test Data to NASA Test Data (Invited), *Proceedings*, 53rd AIAA Aerospace Sciences Meeting, AIAA SciTech, Kissimmee, Florida, AIAA 2015-1093.
[14] NASA Ames Research Center Fluid Mechanics Laboratory: Standard Operating Procedures, Document No. AOX-2010-001 (2010).
[15] http:// http://commonresearchmodel.larc.nasa.gov/geometry/
[16] Schairer, *et al*., Predicting camera views for image-based measurements in wind tunnels, *AIAA* Paper no. 2005-1349.
[17] Čantrak, Đ.S., *et al.*, Laser insight into the turbulent swirl flow behind the axial flow fan, ASME Paper no. GT2014-26563 (2014).
[18] Javadi, A., Nilsson, H., LES and DES of strongly swirling turbulent flow through a suddenly expanding circular pipe, *Computers & Fluids*, 107 (2015), pp. 301-313.
[19] Lumley, J.L., Newman, G.R., The return to isotropy of homogeneous turbulence. *J. Fluid Mech.*, 82 (1977), pp. 161-178.
[20] Lumley, J.L., Choi, K.S., The return to isotropy of homogeneous turbulence, *J. Fluid Mech.*, 436 (2001), pp. 59-84.
[21] Song, K., *et al*., Relaminarization of Wall Turbulence by High-Pressure Ramps at Low Reynolds Numbers, *Thermal Science*, 20 (2016), Suppl. 1, pp. S93-S102

[22] Čantrak, Đ.S., Analysis of the vortex core and turbulence structure behind axial fans in a straight pipe using PIV, LDA and HWA methods, Ph. D. thesis, University of Belgrade, Serbia (2012)

Paper submitted: October 5, 2016
Paper revised: October 22, 2016
Paper accepted: December 22, 2016